Supporting Information

Self-purifying electrolyte enables high energy Li ion batteries

Di Lu,[a] Xincheng Lei,[b] Suting Weng,[b] Ruhong Li,[a] Jiedong Li,[c] Ling Lv,[a] Haikuo Zhang,[a] Yiqiang Huang,[a] Junbo Zhang,[a] Shuoqing Zhang,[a] Liwu Fan,[d] Xuefeng Wang,[b] Lixin Chen,[a,e] Guanglei Cui,[c] Dong Su[b,*] and Xiulin Fan[a,*]

[a]State Key Laboratory of Silicon Materials, School of Materials Science and Engineering, Zhejiang University, Hangzhou 310027, China. E-mail: xlfan@zju.edu.cn

[b]Beijing National Laboratory for Condensed Matter Physics, Institute of Physics, Chinese Academy of Sciences, Beijing 100190, China. E-mail: dongsu@iphy.ac.cn

[c]Qingdao Industrial Energy Storage Research Institute, Qingdao Institute of Bioenergy and Bioprocess Technology, Chinese Academy of Sciences, Qingdao 266101, China.

[d]State Key Laboratory of Clean Energy Utilization, School of Energy Engineering, Zhejiang University, Hangzhou, 310027, China

[e]Key Laboratory of Advanced Materials and Applications for Batteries of Zhejiang Province, Hangzhou 310013, China

Experimental section

1. Preparation of electrolytes and wettability test

Battery-grade lithium bis(fluorosulfonyl)imide (LiFSI) and lithium hexafluorophospate ($LiPF_6$) were purchased from Dadu New Material Co., Ltd. Ethylene carbonate (EC) and Dimethyl carbonate (DMC) were purchased from Duoduo Chem Co., Ltd. Vinylene carbonate (VC) and (2-cyanoethyl)triethoxysilane (TEOSCN) were purchased from TCI. The two reference electrolytes were 1 M $LiPF_6$ EC/DMC (1:1 v/v) (named BE electrolyte) and 1 M $LiPF_6$ EC/DMC (1:1 v/v) + 2 wt.% VC (named BE + 2% VC electrolyte). The LiFSI-TEOSCN electrolyte was prepared by mixing 1.6 M LiFSI salt and TEOSCN solvent. All solvents were dried over activated molecular sieves before use. All electrolytes were prepared in an argon-filled glovebox (Mikrouna, China) with moisture and oxygen contents less than 0.1 ppm. A contact angle facility (JC2000, Shanghai Zhongchen Digital Technic Apparatus Co., Ltd) was utilized to analyze the wettability of electrolyte to Polyethene (PE) separators.

2. Preparation of Electrodes and fabrication of coin cells

The cathode slurry was composed of 80 wt.% $LiNi_{0.8}Mn_{0.1}Co_{0.1}O_2$ (NMC811, Shanghai Chint Power Systems Co., Ltd.), 10 wt.% conductive carbon black (Super C45, Hefei Kejing Materials Technology Co., Ltd), 10 wt.% polyvinylidene fluoride binder (PVDF, Duoduo Chem Co., Ltd.) and N-methyl-2-pyrrolidinone (NMP, Duoduo Chem Co., Ltd.) as solvent, which was coated on aluminum foil. The anode slurry was composed of 93 wt.% graphitic mesocarbon microbeads (MCMB, Hefei Kejing Materials Technology Co., Ltd), 2 wt.% conductive carbon black (Super C45, Hefei Kejing Materials Technology Co., Ltd), 5 wt.% aqueous binder (LA133, Duoduo Chem Co., Ltd.) and pure H_2O as solvent, which was coated on copper foil. After solvent has been dried, the electrodes were punched into disks with diameters of 12 and 14 mm for cathodes and anodes followed by additional vacuum drying at 100 °C overnight prior to the assembling of both half-cells and full-cells, respectively. The mass loading of NMC811 and MCMB for coin-cells were about 6 mg cm^{-2} and 6.2 mg cm^{-2}, respectively. Coin half-cells with as-prepared electrolytes (100 μL) were assembled with NMC811 (or MCMB) as working electrode, lithium foil (Tianjin China Energy Lithium Co., Ltd) as counter electrode, and PE membrane (ND16, SK Innovation Co., Ltd.) as separator. Coin full-cells were fabricated with a set N/P value of 1.2 (calculated according to 200 mA h g^{-1} for NMC811 and 320 mA h g^{-1} for MCMB) using the as-prepared electrolytes (100 μL). For MCMB||NMC811 pouch-type cells (1 Ah) were purchased from LI-FUN Technology Co., Ltd.

3. Electrochemical measurements

The charge/discharge tests of coin-cells and pouch-cells were conducted by LAND system (Wuhan

LAND electronics Co., Ltd.) For coin-type cells, Li||NMC811 and MCMB||NMC811 cells were cycled at 0.1 C rate for first 2 cycles, followed by cycling at 1 C rate charge and 2 C rate discharge under a voltage range of 2.8-4.3 V. Li||MCMB half cells were cycled at 0.1 C rate under a voltage of 0.005-1.5 V. MCMB||$LiCoO_2$ full-cells were performed at 0.1 C rate for first two formation cycles, and then 0.5 C rate for long cycles under 3.0-4.4 V. The rate capability was obtained from MCMB||NMC811 full-cells cycled at constant charge (0.5 C) and different discharge (0.2 C, 0.5 C, 1 C, 2 C, 3 C, 4 C, 5 C). For extreme cases, MCMB||NMC811 cells with different electrolytes exposed in the air for 1 h were cycled at 0.1 C rate for first 5 cycles, followed by cycling at 0.5 C rate charge and discharge under a voltage range of 2.8-4.3 V. For pouch-type cells, MCMB||NMC811 (1 Ah) were cycled at 0.1 C rate for 3 formation cycles, and then 0.3 C charge/discharge for long cycles under 2.8-4.3 V. The linear sweep voltammetry (LSV) was performed to evaluate stable electrochemical windows of three electrolytes. The electrochemical impedance spectroscopy (EIS) of MCMB||NMC811 full-cells at a fully discharged state was measured using an electrochemical workstation (Ivium-n-stat, Ivium Technologies BV Co. Ltd.) over frequencies from 10 kHz to 10 mHz with a voltage amplitude of 10 mV. The electrochemical floating test was performed with Li||NMC811 half-cells in different electrolytes. The cells cycled 100 cycles maintain 5 V for 12 h, and the current was monitored by Ivium-n-stat.

4. Material characterizations

The solvation structures of different concentration electrolytes (sealed in a capillary tube) were studied by Raman spectroscopy (LabRAM HR Evolution, Horiba Jobin Yvon). The Ni/Co/Mn concentration of the fully charged NMC811 cathodes (disassembled from MCMB||NMC811 full-cells cycled 100 cycles at 1 C charge / 2 C discharge) was tested by inductively coupled plasma mass spectrometry (ICP-MS, Agilent 7700). ^{19}F nuclear magnetic resonance spectroscopy (600 MHz NMR, AgilentDD2 600) was used to examine the HF removal effect of obvious electrolytes after added 2 vol.% H_2O and stored 24 h. The cathodes and anodes were disassembled from MCMB||NMC811 full-cells cycled 100 cycles at 1 C charge / 2 C discharge, and rinsed with anhydrous DMC three times to remove the residuals (inside the glovebox). The compositions of electrodes interphase were obtained from X-ray photoelectron spectroscopy (XPS, Escalab 250Xi, Thermo Fisher Scientific). The morphology features of electrodes surface were received from Scanning electron microscope (SEM, SU-70, Hitachi Ltd.). The cross-SEM images of NMC811 were acquired by focused ion beam (FIB, FEI Helios 600i) milling process and the subsequent transmission electron microscopy (TEM) samples were prepared by FIB lift-out method. The structure changes and elemental distributions were characterized from high angle annular dark field (HAADF) images and scanning transmission electron microscopy-electron energy loss spectroscopy (STEM-EELS) images, which were collected by JEOL JEM-ARM200CF with a probe corrector. For anodes, high-resolution

transmission electron microscopy (HRTEM) imaging and STEM-EELS mapping were performed using a JEOL JEM-F200 with an air-tight vacuum transfer holder (Fischione 2550) at -180 °C. The specimens were loaded on a copper grid in argon-filled glove box and transferred into the TEM without any air exposure. In-situ Differential Electrochemical Mass Spectrometry (In-situ DEMS) was performed to explore the gas evolution behaviour of in situ cell (commercial ECC-DEMS cell, EL-CELL GmbH) during charge or discharge process. Herein, porous glass microfiber filter paper (GF/D, Whatman) was used as separator, and argon was selected as inert carrier gas. The equipped mass spectrometer in the DEMS system was HPR-20 (Hiden Analytical Ltd.).

5. Theoretical calculations

5.1. MD simulations

MD simulations were performed in LAMMPS using the all-atom optimized potentials for liquid simulations (OPLS-AA) force-field with the Li^+, and FSI^- anions description from previous publication.[1,2] The electrolyte systems were setup initially with the 256 Li^+ ions, 256 FSI^- ions, and 576 TEOSCN molecules distributed in the simulation boxes (65 Å in length) using Moltemplate (http://www.moltemplate.org/). For the system, an initial energy minimization at 0 K (energy and force tolerances of 10^{-5}) was performed to obtain the ground-state structure. And then, the temperature of system was slowly increased from 0 K to 298 K at constant volume over 0.2 ns using a Langevin thermostat, with a damping parameter of 100 ps. The system was equilibrated in the constant temperature (298 K), constant pressure (1 bar) (NpT ensemble) for 5 ns before finally being subjected to 5 ns of constant volume, constant temperature dynamics. Radial distribution functions were obtained using the Visual Molecular Dynamics (VMD) software. Snapshots of the most probable solvation shells were also sampled from the simulation trajectory using VESTA.

5.2. Periodic calculations

Periodic planewave DFT+U calculations for the electrolyte/cathode interface systems were performed using the Vienna ab initio Simulation Package (VASP) with the spin-polarized Perdew-Burke-Ernzerhof (PBE) exchangecorrelation functional and the projector-augmented wave (PAW) scheme to treat core electrons. A planewave energy cutoff of 500 eV was employed. For the +U augmented treatment of Ni, Co, and Mn 3d orbitals, we chose a U_{eff} (J = 0.0 eV) value of 6.20 eV for Ni, 3.32 eV for Co, and 3.90 eV for Mn. The (001) surface for the 66.6% delithiated $Li_{0.33}N_{i0.8}Co_{0.1}Mn_{0.1}O_2$ structure was generated by removing the Li atoms from the corresponding fully lithiated ($LiNi_{0.8}Co_{0.1}Mn_{0.1}O_2$; O termination) slab structure and re-optimizing. The $Li_{0.33}Ni_{0.8}Co_{0.1}Mn_{0.1}O_2$ (001) slab consists of 8 layers and a 15 Å vacuum layer in the z-direction. All selected molecules were put on the cathode surface in multiple orientations, with some of the H atoms pointing towards surface O atoms. In a second set of calculations, one H atom from the solvent was transferred to the closest surface O, and the geometry was optimized again. We set

the energy convergence criteria to 10^{-6} eV A^{-1}, and forces were converged below 0.01 eV $Å^{-2}$ during geometry optimization.

5.3. Quantum chemistry calculations

The density functional theory (DFT) implanted in Gaussian 09 software was used to perform the quantum chemistry calculations. The equilibrium state structures with geometry optimization were performed by employing three-parameter empirical formulation B3LYP in conjunction with the basis set of 6-311+G (d, p).[2-4] Calculations were performed under the gas phase approximation. The absence of imaginary frequencies is in the calculated vibrational frequencies of the optimized structures to ensure stable structures. Then the free energy of the reactants and products were used to calculate the ΔG of proposed reactions.

Results and discussion

Table S1. Probability and number of FSI^- and TEOSCN in 1.6 M LiFSI TEOSCN electrolyte within a cut-off distance of 4.6 Å from the Li ions calculated from MD simulations.

Number of FSI^- ions	Probability (%)	Number of TEOSCN ions	Probability (%)
0	3.52	0	1.17
1	22.66	1	15.63
2	41.41	2	44.53
3	23.44	3	26.56
4	8.60	4	12.11
5	0.39		
Average number	2.121		2.328

Table S2. Surface resistance (R_s), charge transfer resistance (R_{ct}) and interfacial resistance (R_i) of MCMB||NMC811 full-cells using different electrolytes corresponding to the EIS data of fitting equivalent circuit in Figure S8.

Electrolyte	Cycle	100th	500th	1000th	Increment (Ohm)
BE	R_s (Ohm)	5.5	7.1	10.1	
	R_{ct} (Ohm)	56.5	87.4	93.3	
	R_i (Ohm)	62.0	94.5	103.4	41.4
BE + 2% VC	R_s (Ohm)	6.4	7.2	9.1	
	R_{ct} (Ohm)	56.7	44.4	67.8	
	R_i (Ohm)	63.1	51.6	76.9	13.8
LiFSI-TEOSCN	R_s (Ohm)	4.2	4.7	6.1	
	R_{ct} (Ohm)	27.8	25.5	29.7	
	R_i (Ohm)	32.0	30.2	35.8	3.8

Table S3. Characterization analysis of NMC811 cathodes recovered from MCMB||NMC811 full-cells after 100 cycles using different electrolytes.

Electrolyte	FIB-SEM	HAADF	ABF	EELS	
	Degree of secondary particle crack	Rock-salt layer thickness	Amorphous layer thickness	Chemical shift of Ni-L_3 from surface to bulk	
				Peak-summit shift	Peak-onset shift
BE	Severe	8 nm	4 nm	858.9-860.5 eV (1.6 eV)	857.0-857.5 eV (0.5 eV)
BE + 2% VC	Middle	4 nm	2 nm	859.0-860.5 eV (1.5 eV)	857.0-857.5 eV (0.5 eV)
LiFSI-TEOSCN	Slight	0 nm	1 nm	860.0-860.6 eV (0.6 eV)	857.2-857.3 eV (0.1 eV)

Table S4. Rietveld refinement results of pristine NMC811 cathode and NMC811 cathodes recovered from MCMB||NMC811 full-cells after 100 cycles using different electrolytes.

NMC811	a axis(Å)	c axis(Å)	Vol ($Å^3$)	R_{wp}	R_p	χ^2
Pristine	2.6867	13.2351	82.7363	0.065	0.053	1.46
BE	2.8162	14.0450	96.4671	0.070	0.059	1.57
BE + 2% VC	2.7571	13.8325	91.0618	0.068	0.057	1.48
LiFSI-TEOSCN	2.7255	13.3592	85.9416	0.059	0.049	1.39

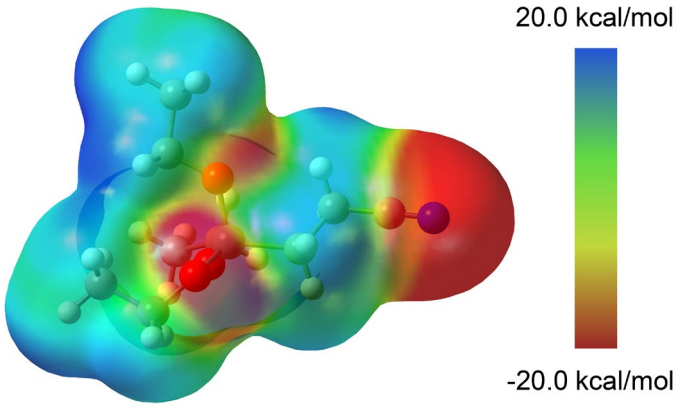

Figure S1. Electrostatic potential diagram of TEOSCN.

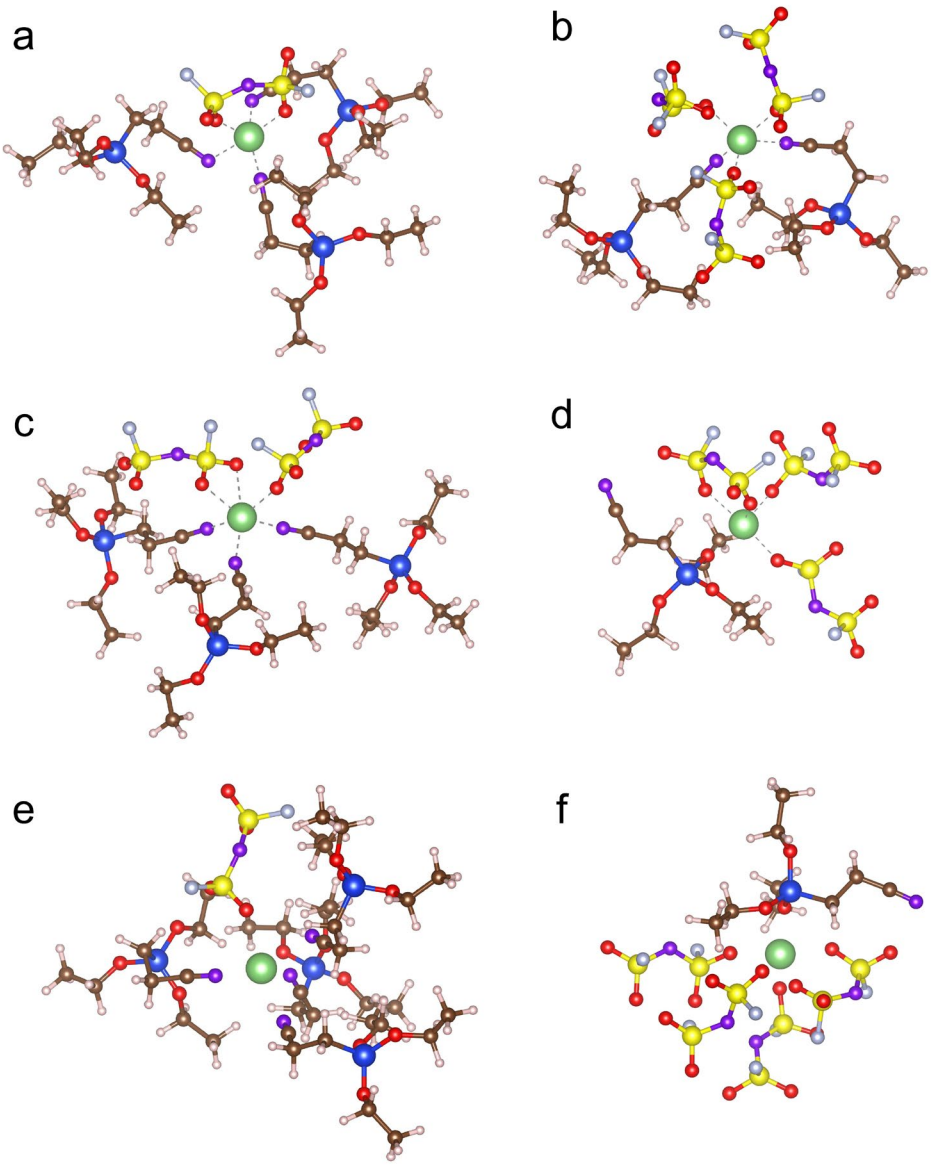

Figure S2. Optimized Li^+ solvation structures of 1.6 M LiFSI-TEOSCN electrolyte in descending order of proportions. (a) 1-FSI^- 3-TEOSCN solvation structure accounts for 14.06%, (b) 3-FSI^- 2-TEOSCN solvation structure accounts for 12.50%, (c) 2-FSI^- 3-TEOSCN solvation structure accounts for 10.16%, (d) 3-FSI^- 1-TEOSCN solvation structure accounts for 8.20%, (e) 1-FSI- 4-TEOSCN solvation structure accounts for 7.03%, (f) 4-FSI- 1-TEOSCN solvation structure accounts for 5.86% (green: Li atom, red: O atom, yellow: S atom, purple: N atom, silver: F atom, blue: Si atom, tan: C atom, white: H atom).

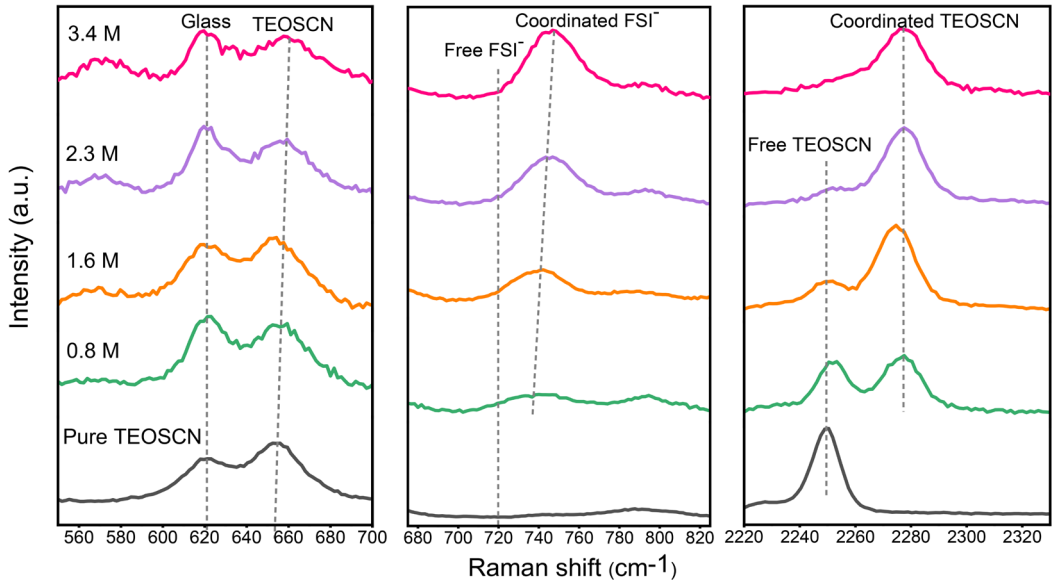

Figure S3. Raman spectra of various concentrations of LiFSI-TEOSCN electrolytes in the range of 550-700 cm^{-1}, 675-825 cm^{-1} and 2220-2330 cm^{-1}.

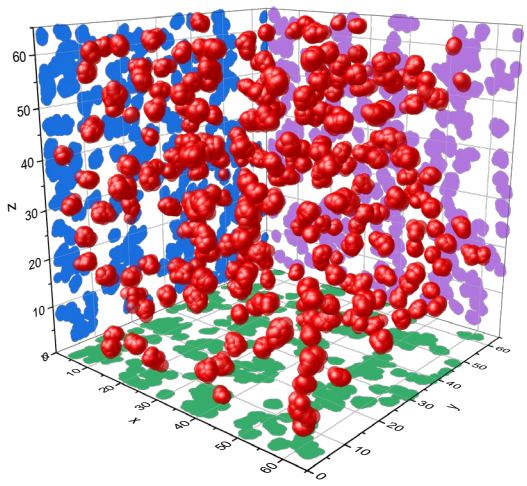

Figure S4. Three-dimensional network diffusion channel of Lithium ions in LiFSI-TEOSCN electrolyte calculated from MD simulation.

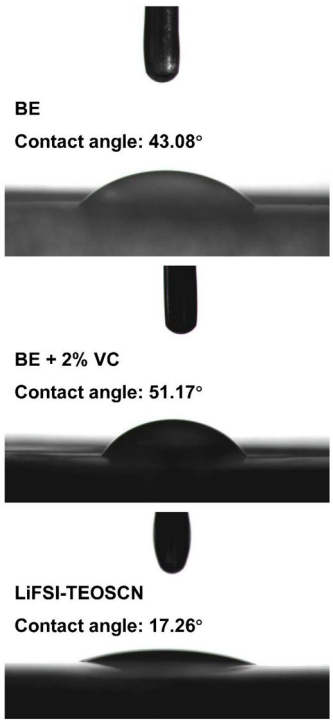

Figure S5. Wettability test of different electrolytes with the PE separators.

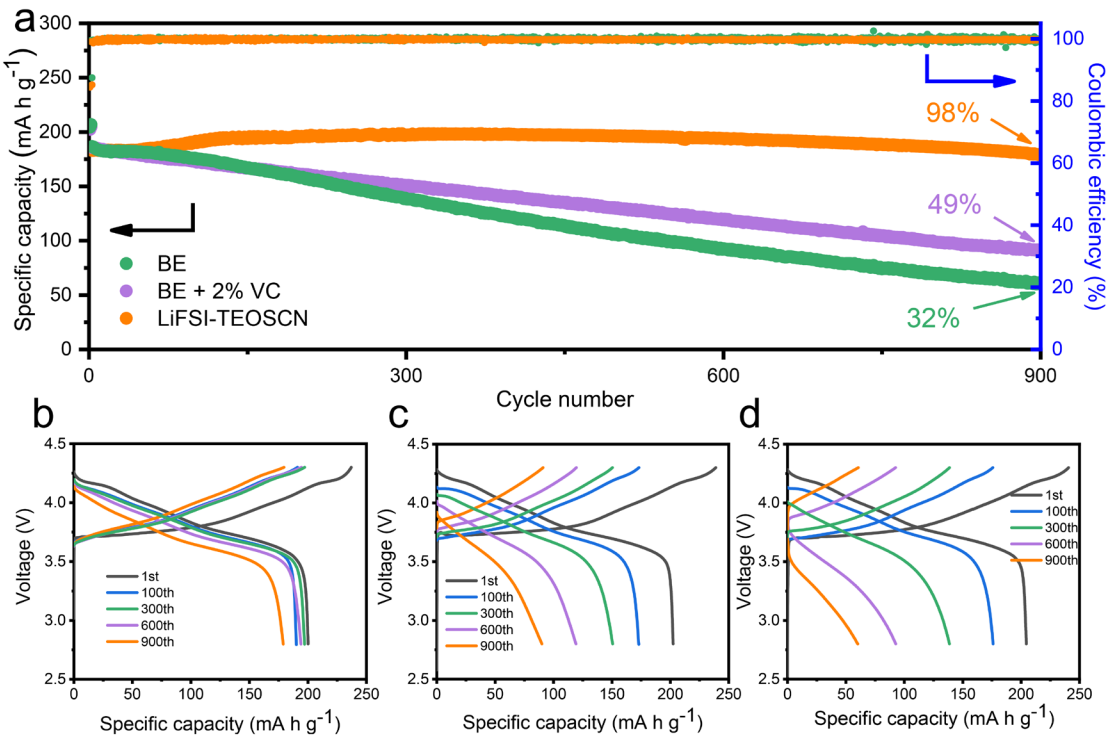

Figure S6. Electrochemical performances of Li||NMC811 half-cells using different electrolytes. (a) Cycling performance of Li||NMC811 half-cells using different electrolytes under 1 C charge and 2 C discharge between 2.8 V to 4.3 V. Voltage profiles of Li||NMC811 half-cells using LiFSI-TEOSCN (b), BE + 2% VC (c) and BE (d) electrolytes between 2.8 V to 4.3 V.

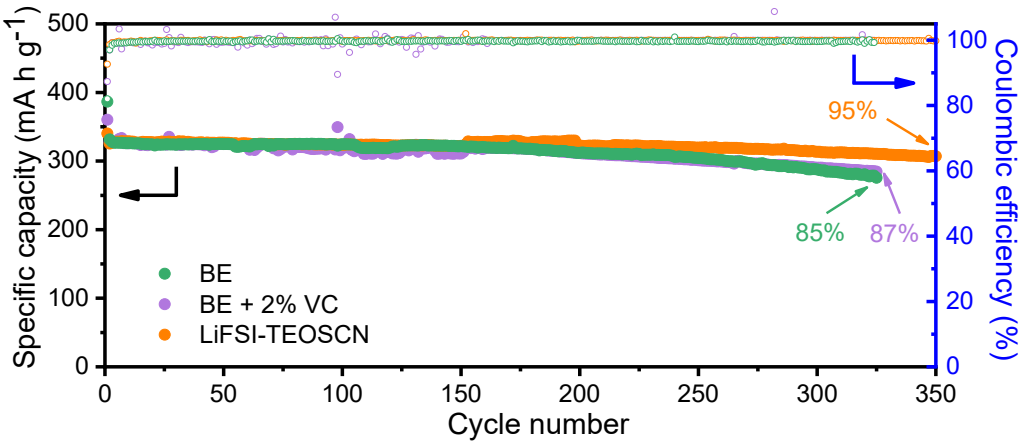

Figure S7. Cycling performance and Coulombic efficiency of Li||MCMB half-cells using different electrolytes under 0.1 C charge and discharge between 0.005 V to 1.5 V.

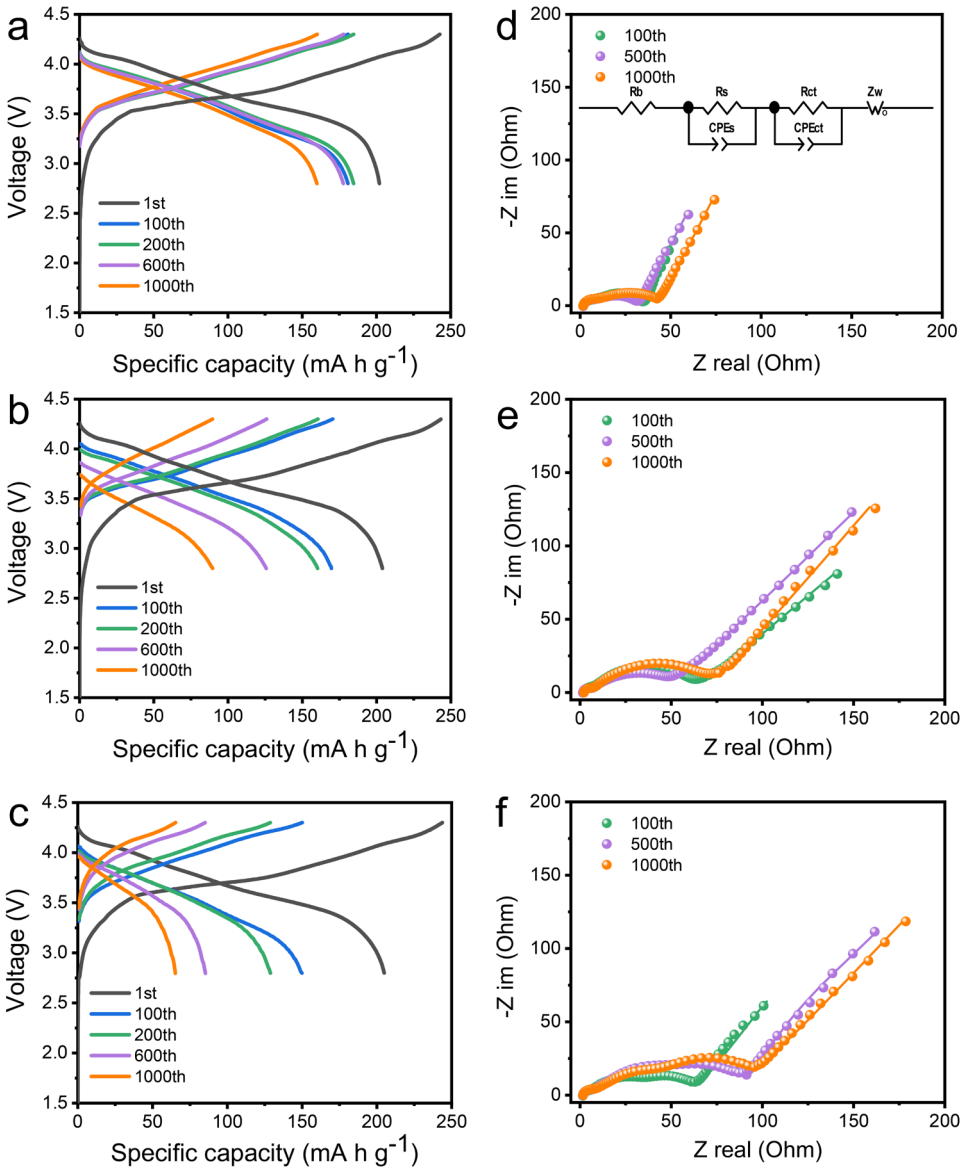

Figure S8. Voltage profiles and Electrochemical impedance spectra of MCMB||NMC811 full-cells using LiFSI-TEOSCN (a, d), BE + 2% VC (b, e) and BE (c, f) electrolytes between 2.8 V to 4.3 V. In electrochemical impedance spectra, the solid lines represent the fits using an equivalent circuit shown in the EIS plot (inset of Figure S6d).

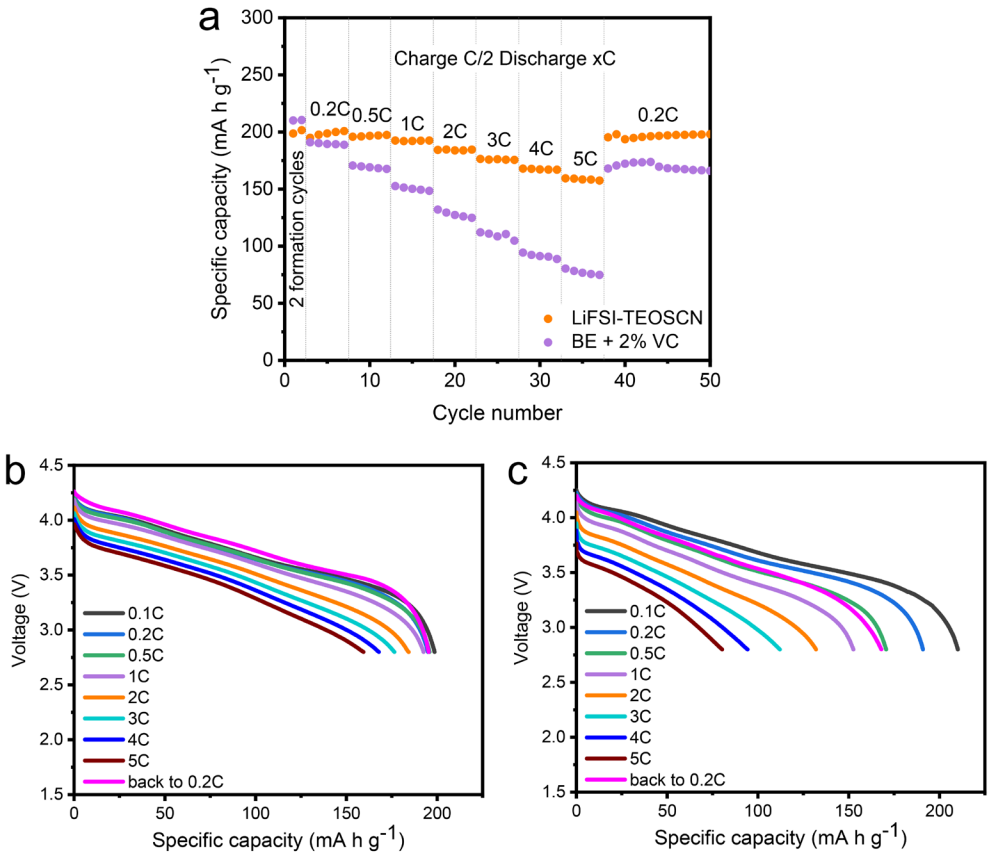

Figure S9. Rate capabilities of different electrolytes in MCMB||NMC811 full-cells under varying discharge rates (*x*C) with the same charge rate at C/2 (a) and discharge curves of MCMB||NMC811 full-cells using LiFSI-TEOSCN (a) and BE + 2% VC (b) electrolytes.

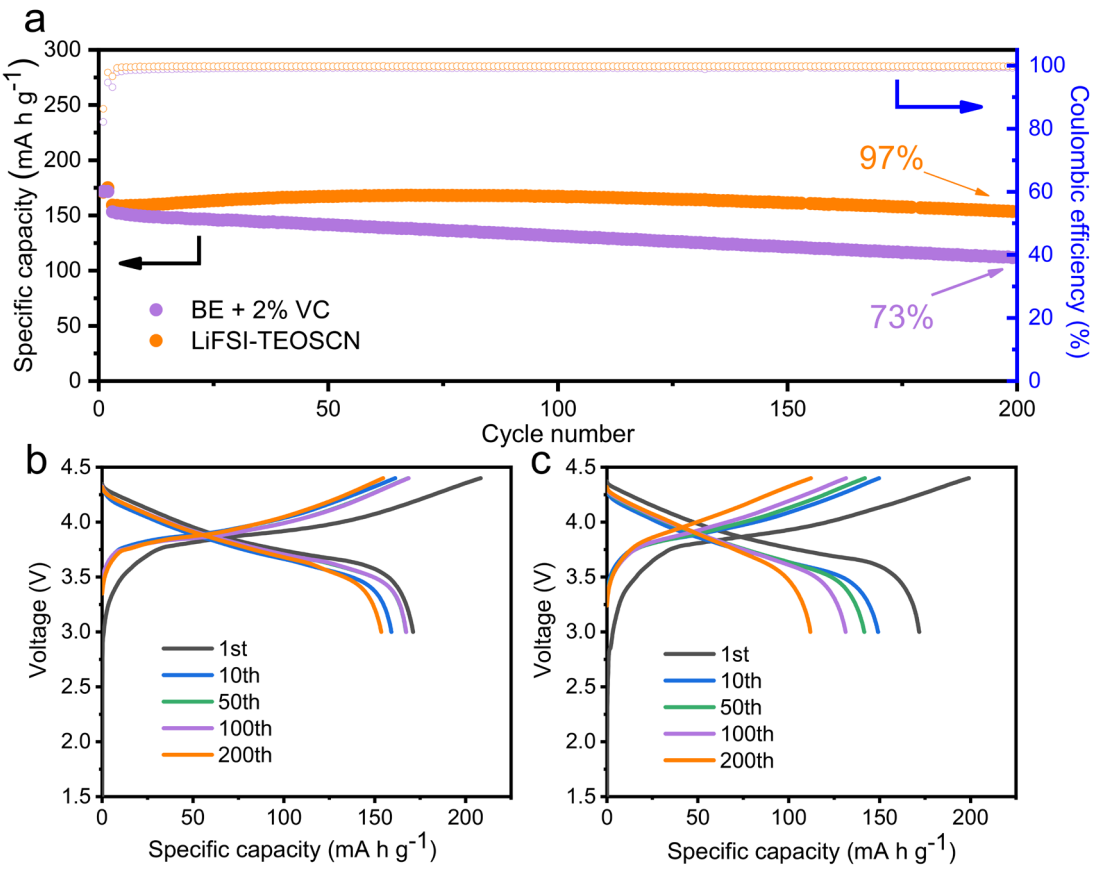

Figure S10. Electrochemical performances of MCMB||$LiCoO_2$ full-cells using different electrolytes. (a) Cycling performance of MCMB||$LiCoO_2$ full-cells using different electrolytes under 0.5 C charge/discharge between 3 V to 4.4 V. Voltage profiles of MCMB||$LiCoO_2$ full-cells using LiFSI-TEOSCN (b) and BE + 2% VC (c) electrolytes.

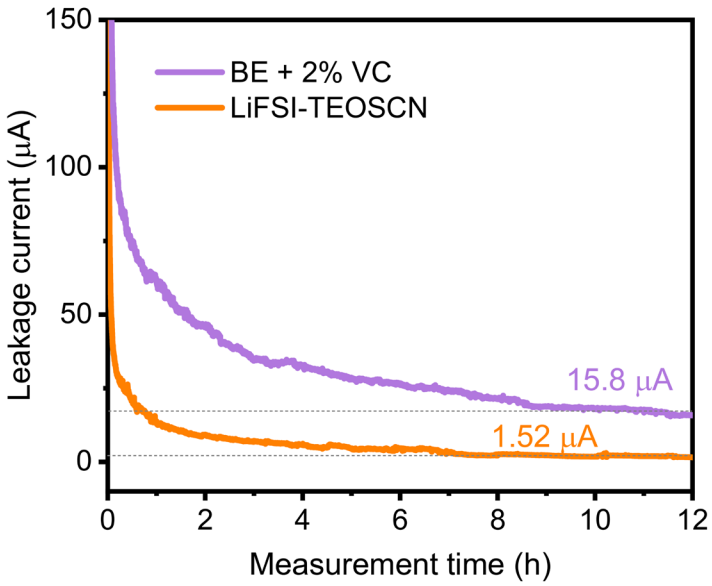

Figure S11. Leakage currents during 5 V constant-voltage floating test of the NCM811 cathodes after 100 cycles.

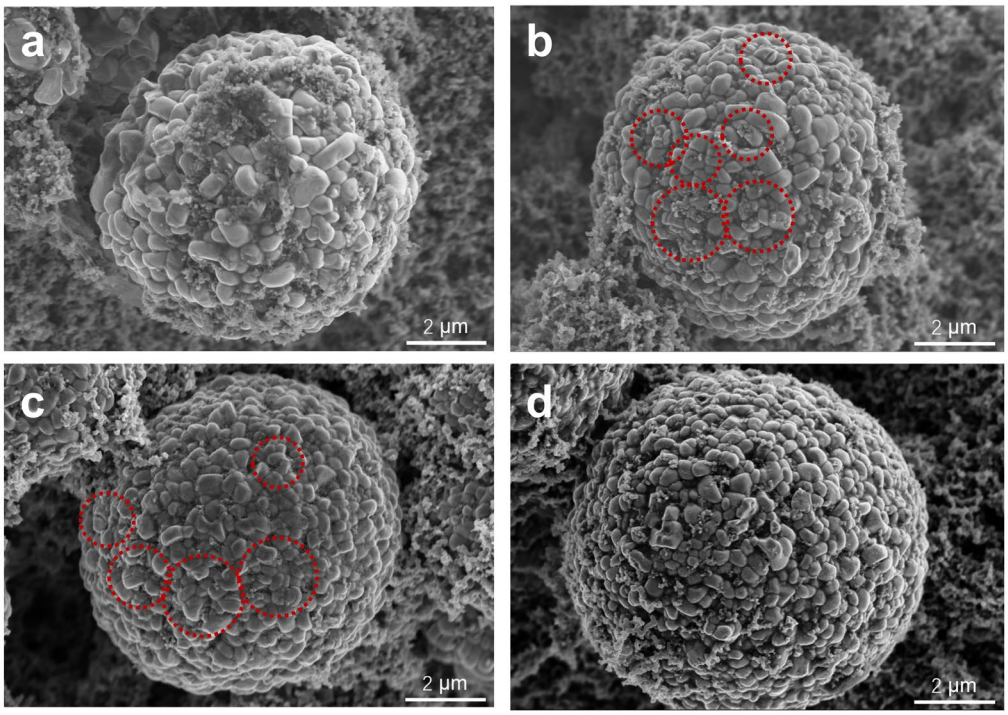

Figure S12. Typical SEM images of uncycled NCM811 electrode (a), and cycled NCM811 electrodes recovered from MCMB||NMC811 full-cells after 100 cycles using BE (b), BE + 2% VC (c) and LiFSI-TEOSCN (d), respectively. The red circles represent the cracks.

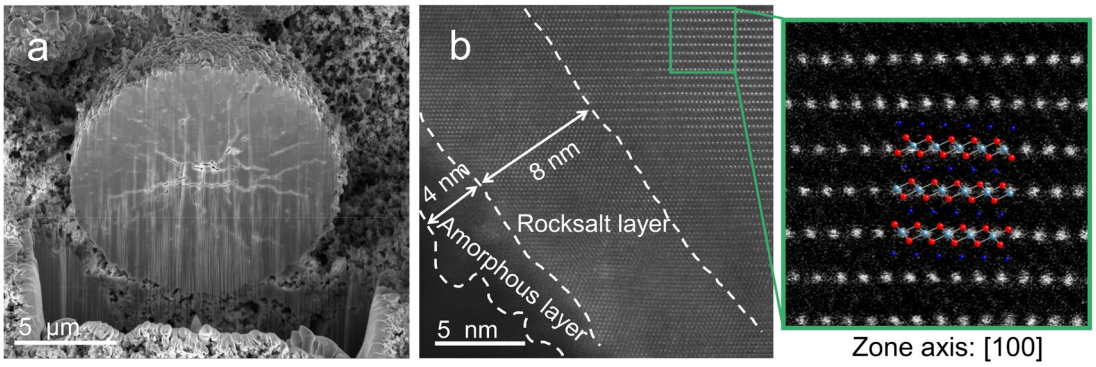

Figure S13. Cross-sectional SEM image (a) and STEM-HAADF image (b) of NMC811 cathode of MCMB||NMC811 full-cell using BE electrolyte after 100 cycles.

After cycling, NMC811 particles in BE electrolyte have more severe internal cracks than those in BE + 2% VC and LiFSI-TEOSCN electrolyte, which corresponds to a rapid degradation of MCMB||NMC811 full-cell with BE electrolyte. Furthermore, about 8 nm cation-mixed rock-salt phase and 4 nm amorphous layer were obviously observed at the surface of NMC811 particles, indicating the grievous surface phase transformation.

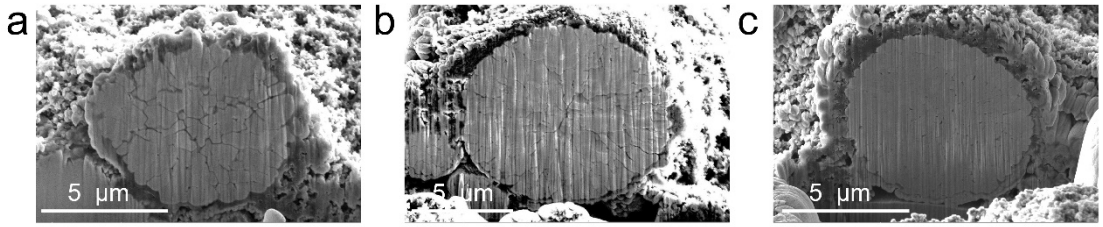

Figure S14. Cross-sectional SEM images of NMC811 cathodes recovered from MCMB||NMC811 full-cells after 1000 cycles using BE (a), BE + 2% VC (b) and LiFSI-TEOSCN (c) electrolytes.

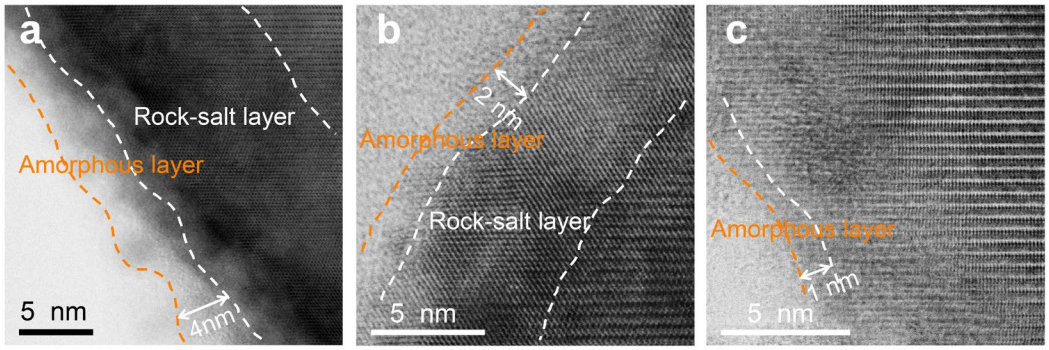

Figure S15. Typical ABF-STEM images of cycled NMC811 cathodes of MCMB||NMC811 cells with electrolytes of BE (a), BE + 2% VC (b) and LiFSI-TEOSCN (c) after 100 cycles.

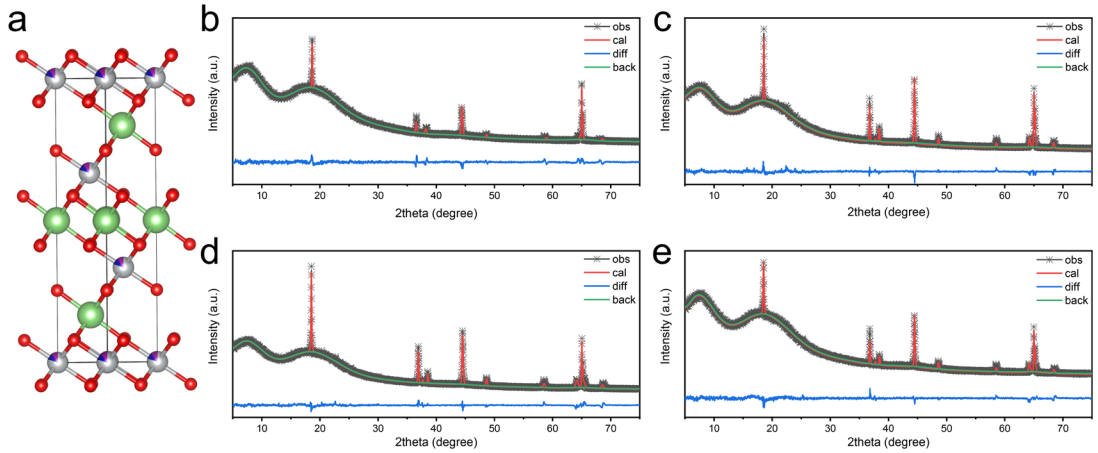

Figure S16. XRD refinement patterns of pristine NMC811 (b) and NMC811 cathodes recovered from MCMB||NMC811 full-cells after 100 cycles using BE (c), BE + 2% VC (d) and LiFSI-TEOSCN (e) electrolytes. The refinement was conducted on the $R\bar{3}m$ (166) phase of LiTMO2 (a).

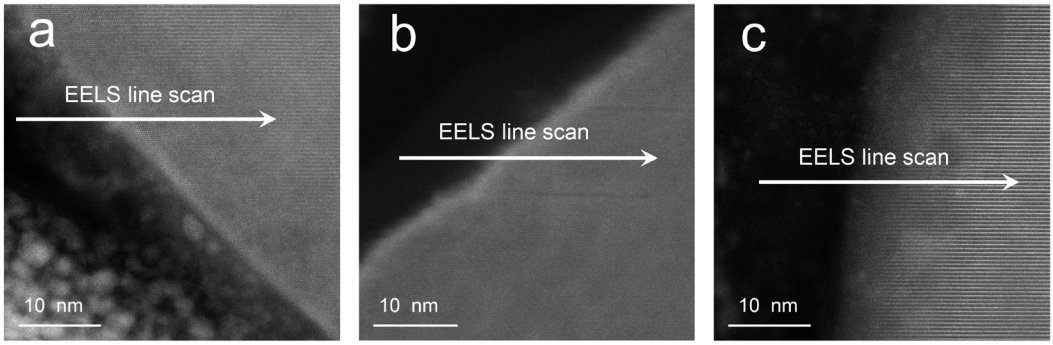

Figure S17. The EELS scanline of the NMC811 particles recovered from MCMB||NMC811 full-cells after 100 cycles using BE (a), BE + 2% VC (b) and LiFSI-TEOSCN (c) electrolytes.

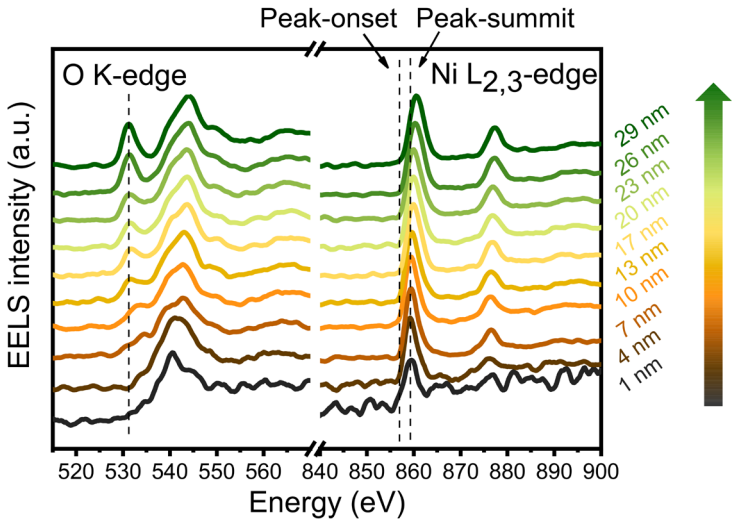

Figure S18. STEM-EELS line scan on the surface of NMC811 cathode of MCMB||NMC811 full-cells using BE electrolyte after 100 cycles.

The pre-edge peak of the O *K*-edge at ~531.0 eV is attributable to the transition of electrons from the O 1*s* state to the O 2*p* state hybridized with the 3*d* state of a TM, while the main peak (~ 541.0 eV) corresponds to the O 1*s* to hybridized O 2*p* and TM 4*sp* states. The occurrence of O-*K* pre-peak at 10-13 nm from particle surface indicates about 10 nm rock-salt phase, while Ni $L_{2,3}$ peaks greatly increase to higher energy from surface to bulk, indicating that thick rock-salt phase and serious defects of O-sub-lattice exist in NMC811 cathode cycled in BE electrolyte.

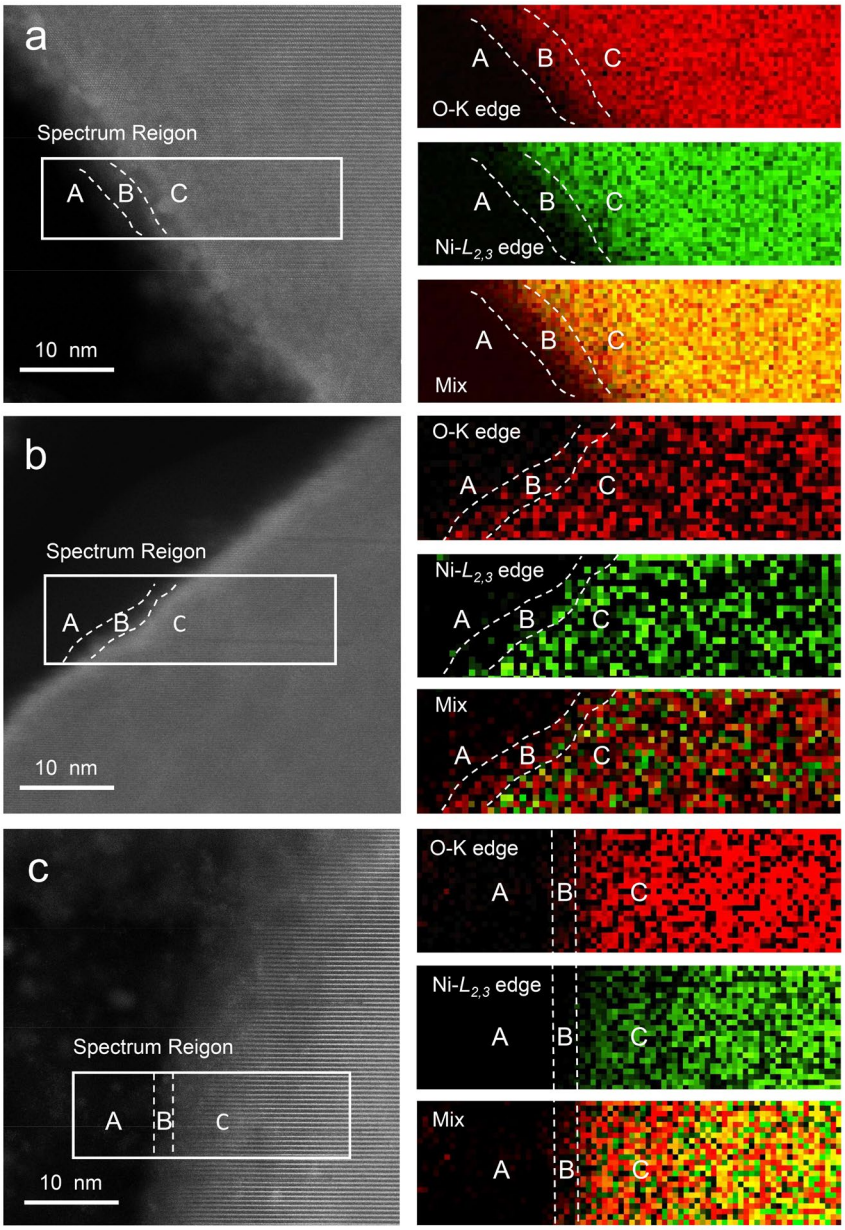

Figure S19. STEM-EELS mappings of NMC811 cathodes of MCMB||NMC811 full-cells using BE (a), BE + 2% VC (b) and LiFSI-TEOSCN (c) electrolytes after 100 cycles.

O-*K* edge signals represent vacuum from amorphous layer, and Ni-$L_{2,3}$ signals represent amorphous layer and particle. EELS mappings clearly divide the region into three parts (A: Vacuum, B: Amorphous Layer, C: NMC811). In different electrolytes, the thickness of amorphous layer on NMC811 cathodes shows a downward trend: BE >BE + 2% VC >LiFSI-TEOSCN electrolyte, which agree with HAADF imaging results and EIS results.

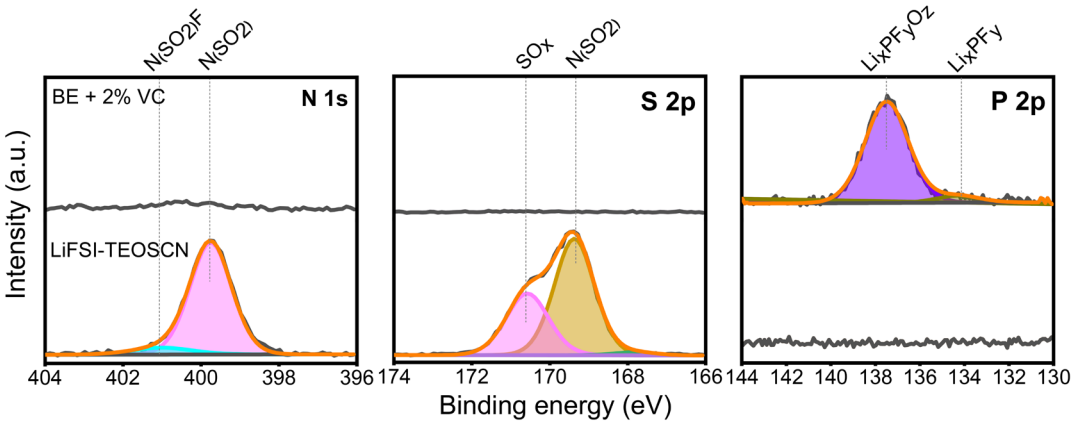

Figure S20. XPS N 1s, S 2p and P 2p spectra for NCM811 cathodes recovered from MCMB||NMC811 full-cells after 100 cycles in different electrolytes.

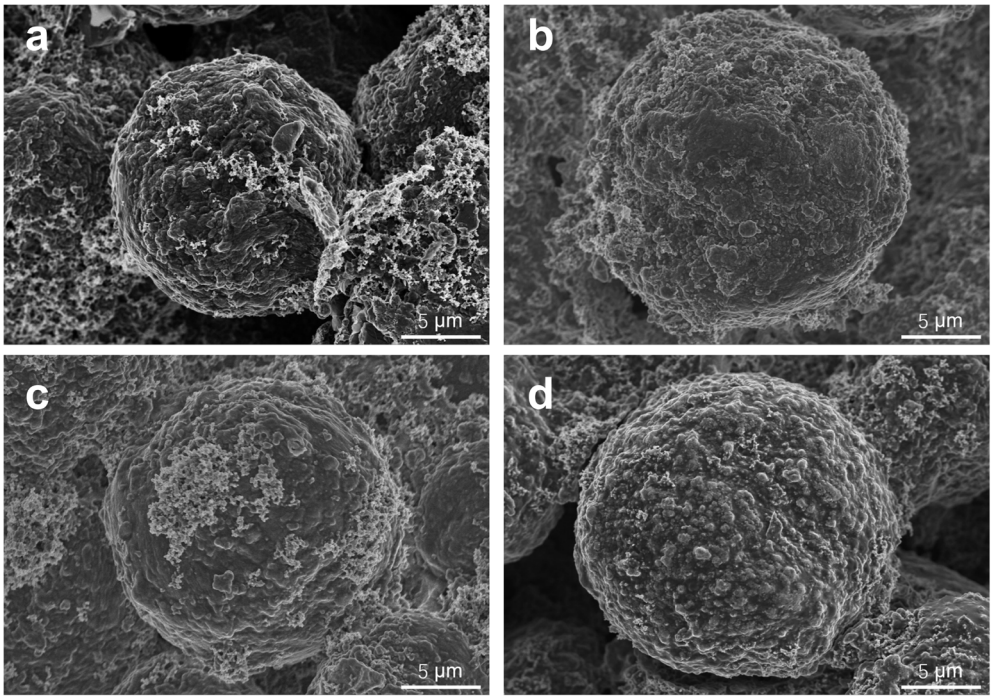

Figure S21. Typical SEM images of uncycled MCMB electrode (a), and cycled MCMB electrodes recovered from MCMB||NMC811 full-cells after 100 cycles using BE (b), BE + 2% VC (c) and LiFSI-TEOSCN (d) electrolytes.

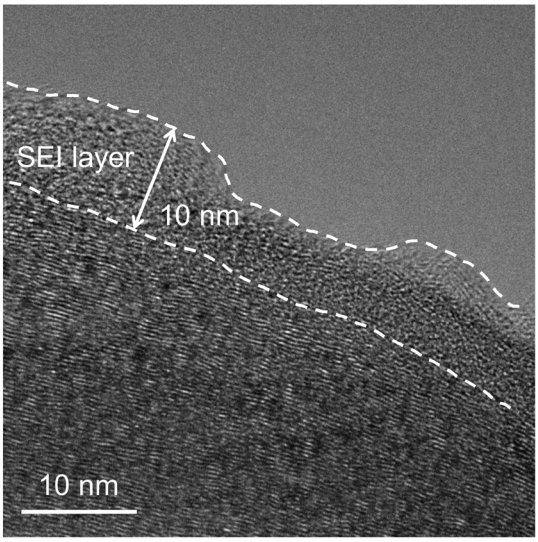

Figure S22. Cryo-HRTEM image of MCMB anode of MCMB||NMC811 full-cell using BE electrolyte after 100 cycles.

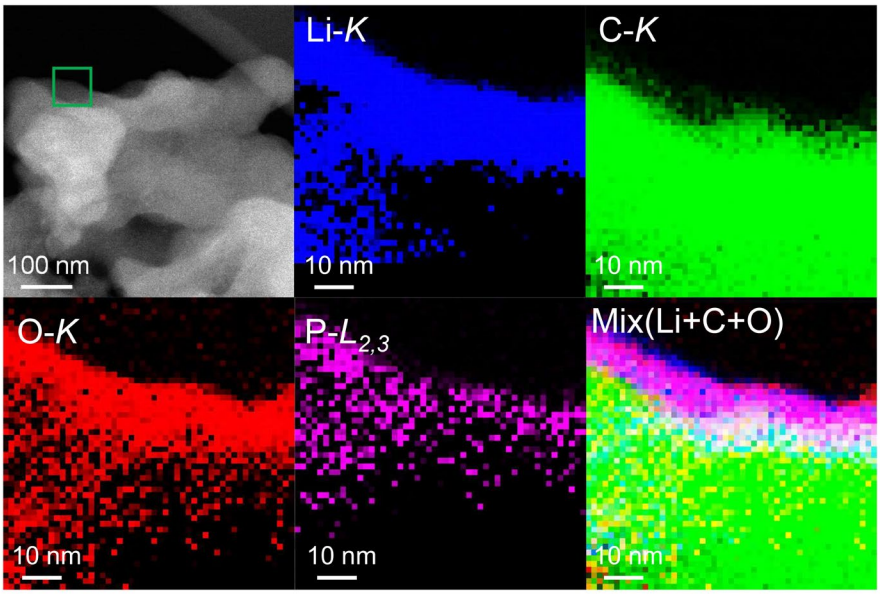

Figure S23. STEM-EELS mapping of MCMB anode of MCMB||NMC811 full-cell using BE electrolyte after 100 cycles.

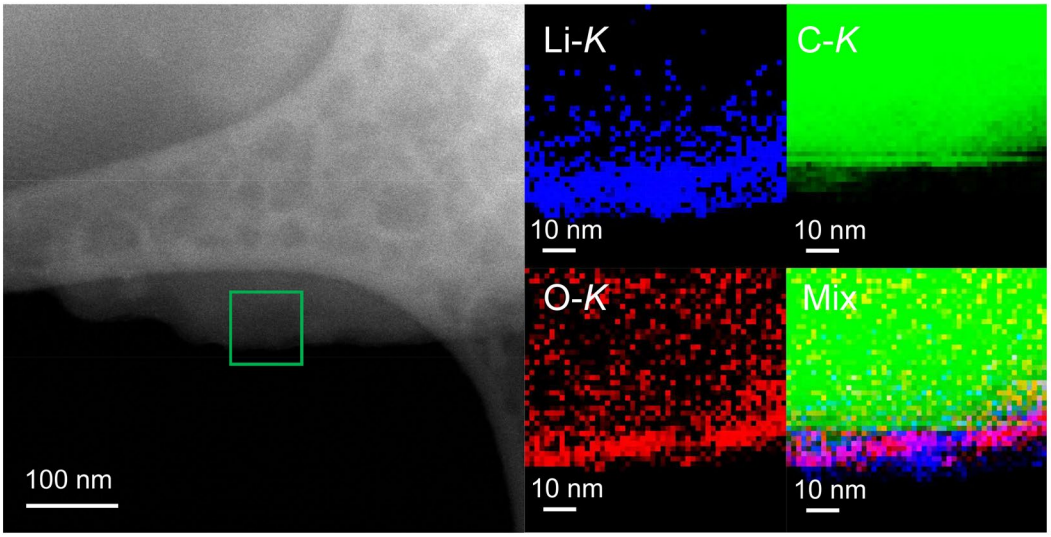

Figure S24. STEM-EELS mapping of MCMB anode of MCMB||NMC811 full-cell using BE + 2% VC electrolyte after 100 cycles. Due to the poor signal-to-noise ratio, STEM-EELS mapping of P is not provided.

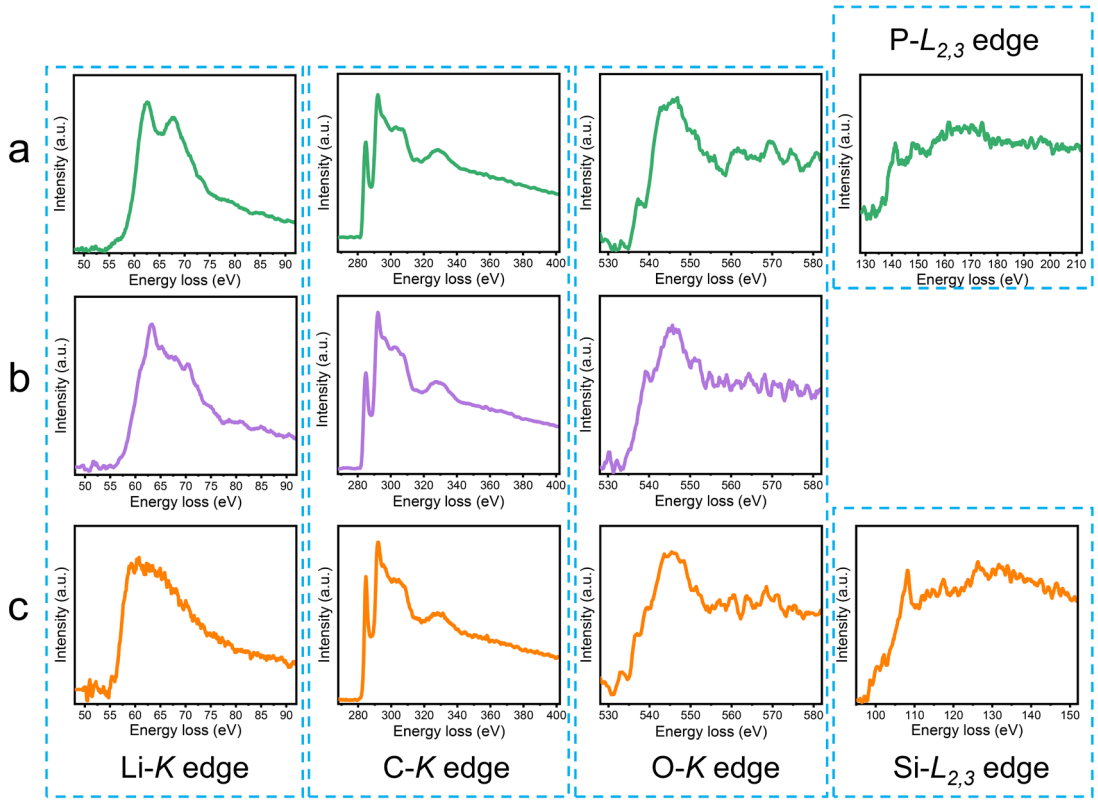

Figure S25. STEM-EELS spectra of MCMB anodes recovered from MCMB||NMC811 full-cells using BE (a), BE + 2% VC (b) and LiFSI-TEOSCN (c) electrolytes after 100 cycles.

From Figure S18-20, Li/C/O EELS mapping and STEM-EELS line scan further provide evidence for SEI layer, which are consistent with the Cryo-HRTEM and XPS results.

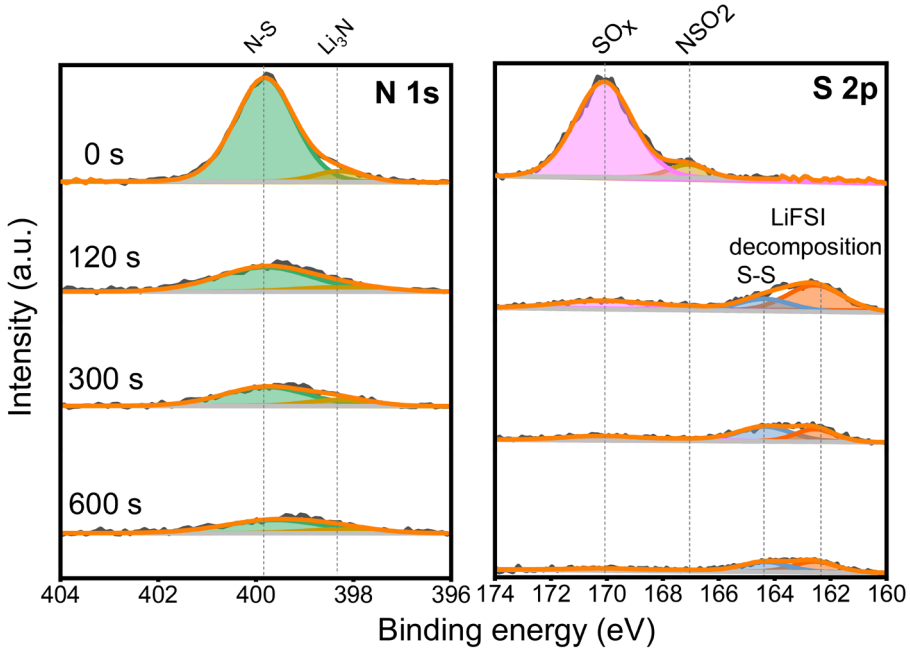

Figure S26. XPS N 1s and S 2p spectra for MCMB anode recovered from MCMB||NMC811 full-cell after 100 cycles using LiFSI-TEOSCN electrolyte.

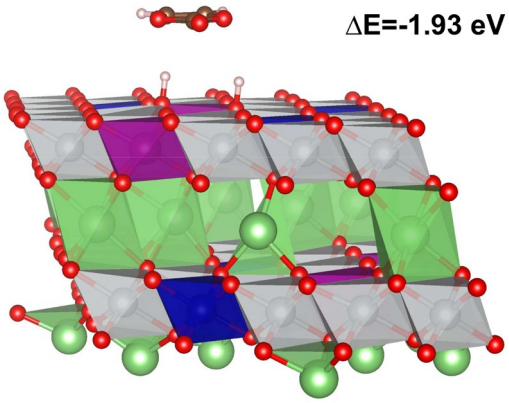

Figure S27. H-transfer reaction from EC (-H) to the NCM811 cathode surface from periodic DFT calculations.

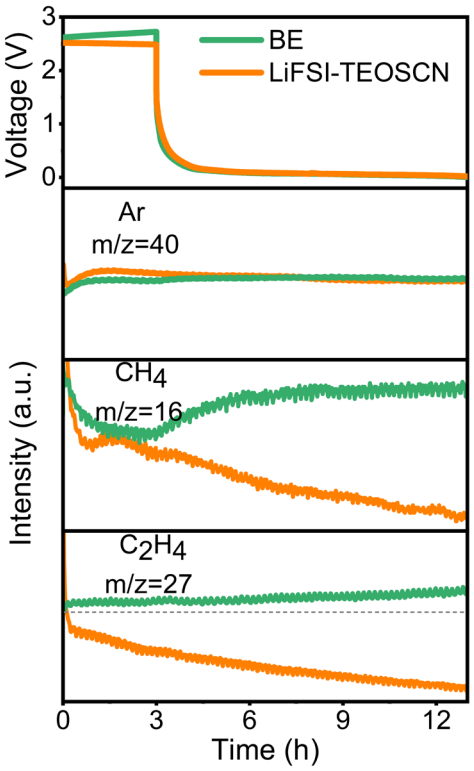

Figure S28. First discharge curve and in situ DEMS signals of Li||MCMB half-cells using different electrolytes.

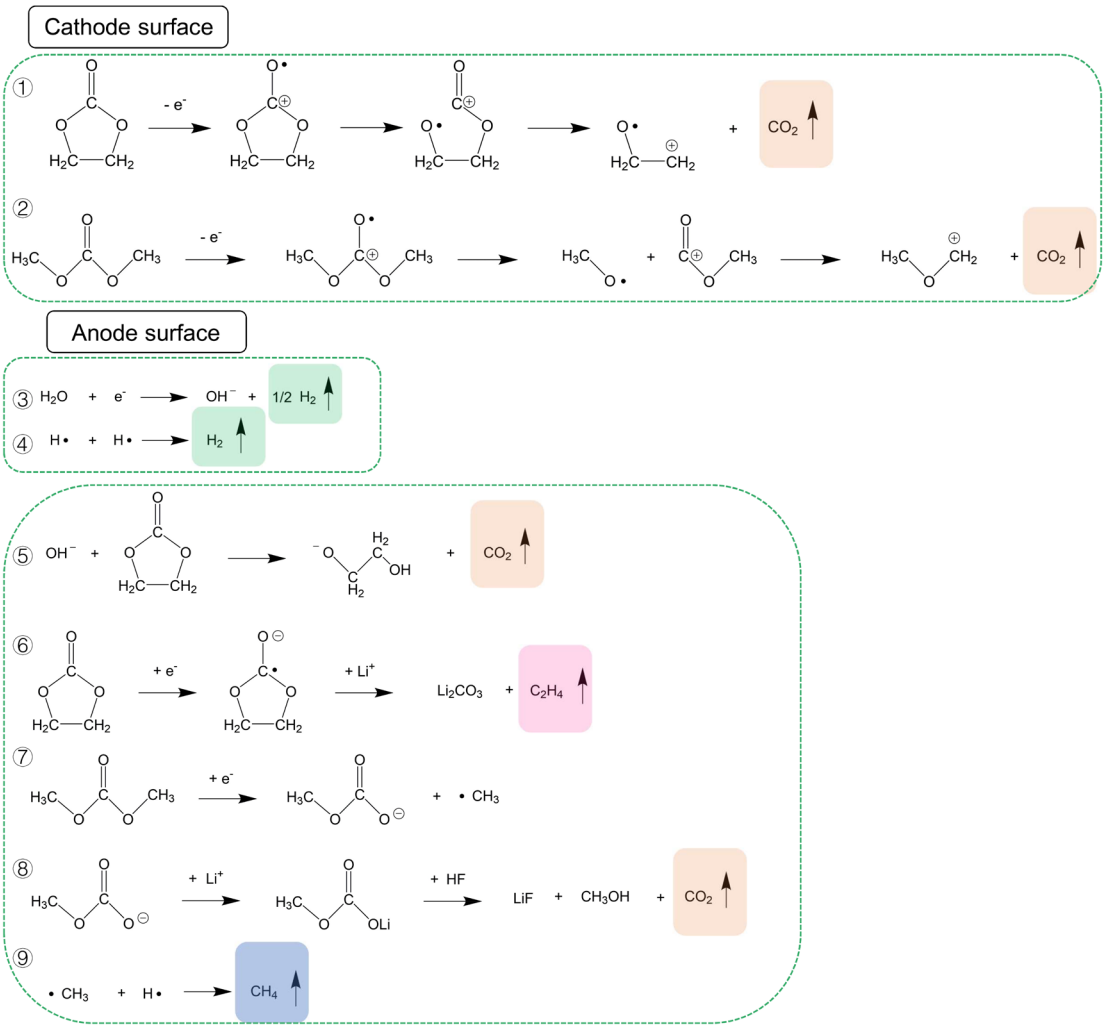

Figure S29. The proposed possible decomposition pathways of BE electrolyte on NCM811 cathode and MCMB anode surface.

Gas evolution is typically crucial in the first cycle with CEI/SEI formation, and continues with cycling, which is closely related to cells performance.[5-7] On cathode surface, EC and DMC occur oxidative decomposition in BE electrolyte (path 1 and 2),[8] generating CO_2 (m/z = 44) which is in line with Figure 5e. On anode surface, unavoidable water impurities and decomposition products cause the production of large amounts of H_2 (m/z = 2) (path 3 and 4). OH^- produced by trace water reduction catalyze EC hydrolysis reaction (Figure 5f) (path 5).[9] Meanwhile, C_2H_4 (m/z = 27) (Figure S24) is also generated from EC and DMC reductive decomposition (path 6-9).[10,11]

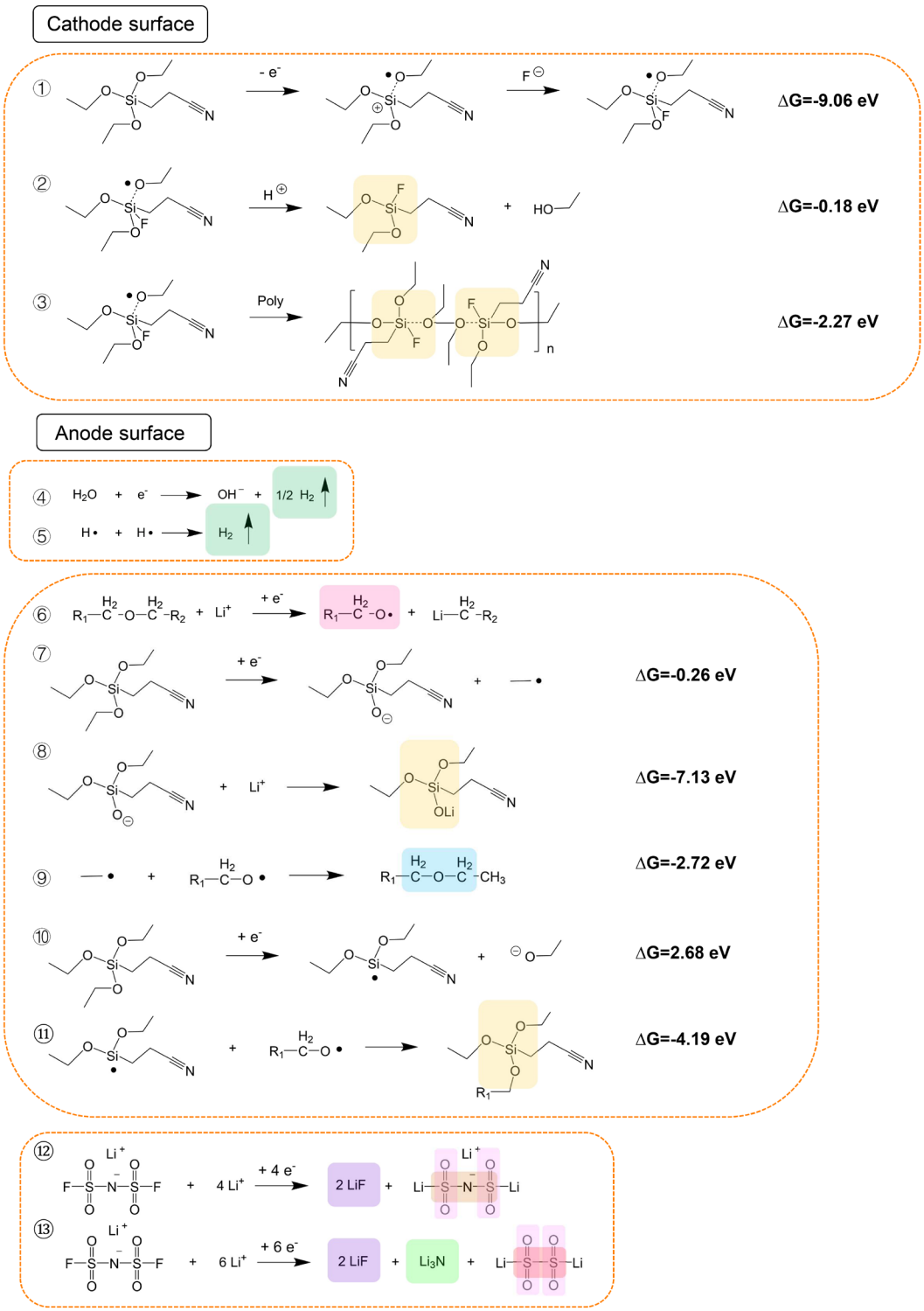

Figure S30. The proposed possible decomposition pathways of LiFSI-TEOSCN electrolyte on NCM811 cathode and MCMB anode surface. The reaction energy was calculated by QC calculations.

In LiFSI-TEOSCN electrolyte, TEOSCN is prone to lose electron and then scavenge F^- (which originated from HF or LiFSI) on the cathode surface as shown in path 1. What's more, the product

will be further oxidized and self-polymerized (path 2 and 3). On anode surface, trace amounts of water generate H_2 (m/z = 2) (Figure 5f) as path 4 and 5. Plenty of C-O-C species are easy to get electrons and produce radical R_1-C-O• (path 6) on MCMB surface.[7] For TEOSCN solvents, the C-O bonds is likely to break (path 7), which further generate Si-O species (path 8) and C-O-C species (path 9). Additionally, XPS results (C-O-C (286.6 eV, C 1s, Figure 4e), C-O-C (532.5 eV, O 1s), Si-O (531.5 eV, O 1s) and Si species (102.1 eV, Si 2p)) and QC calculations (the reaction energy of path 4-6 are lower than path 10) also confirm the correctness of TEOSCN decomposition path. It is worth noting that QC calculations do not admit that path 7 is completely unfeasible, but it is relatively difficult to perform. For LiFSI, the peak of LiF (685 eV, F 1s, Figure 4e), N (N-S, 399.8 eV and Li_3N, 398.2 eV, N 1s, Figure S22), S-O (529.9 eV, O 1s) and S (SO_x, 170.1 eV, NSO_2, 167.0 eV and S-S, 164.3 eV, S 2p) forcefully proved the feasibility of path 12 and 13.[12,13]

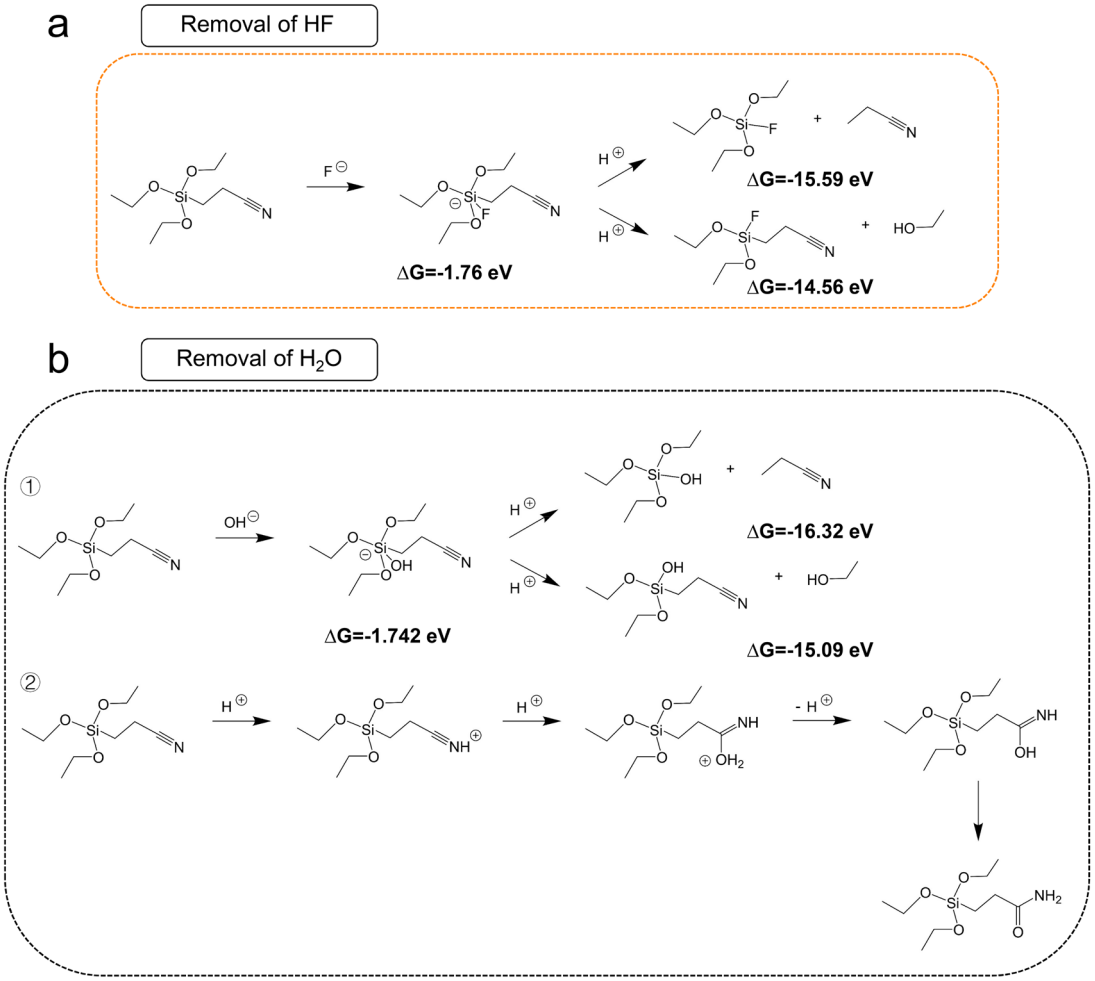

Figure S31. Possible mechanism for HF removal and H_2O removal by TEOSCN solvent.

Actually, the TEOSCN solvent can serve as HF coordination site through formation of Si-F bonds, as demonstrated in Figure S27a, which also proved by QC calculations. Similarly, removal of H_2O resembles that of HF as shown in path 1 of Figure S27b. As for path 2, it is a typical reductive reaction of the nitriles to amides, which can also be regarded as a possibility of TEOSCN decomposition.

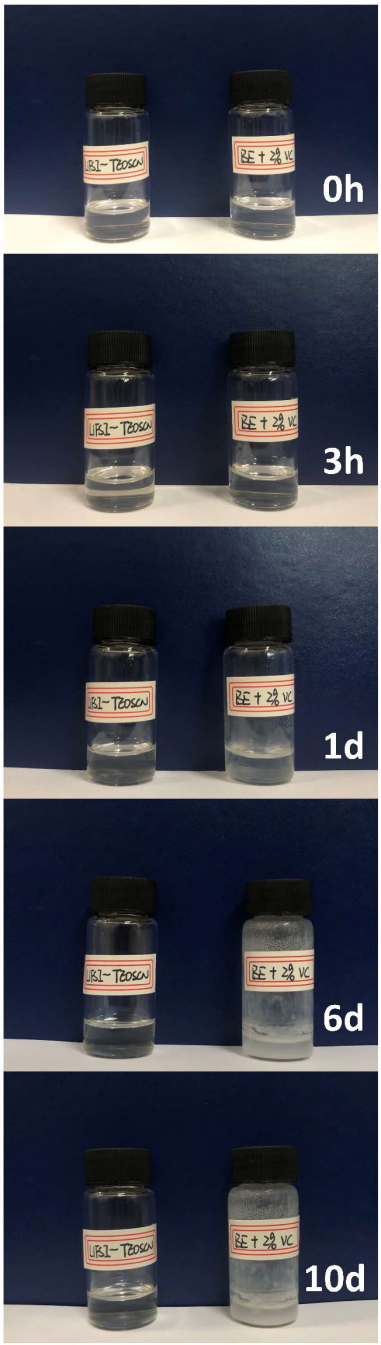

Figure S32. Photographs of LiFSI-TEOSCN and BE + 2% VC electrolyte before and after storage for different times at 25 ℃ and 50% humidity.

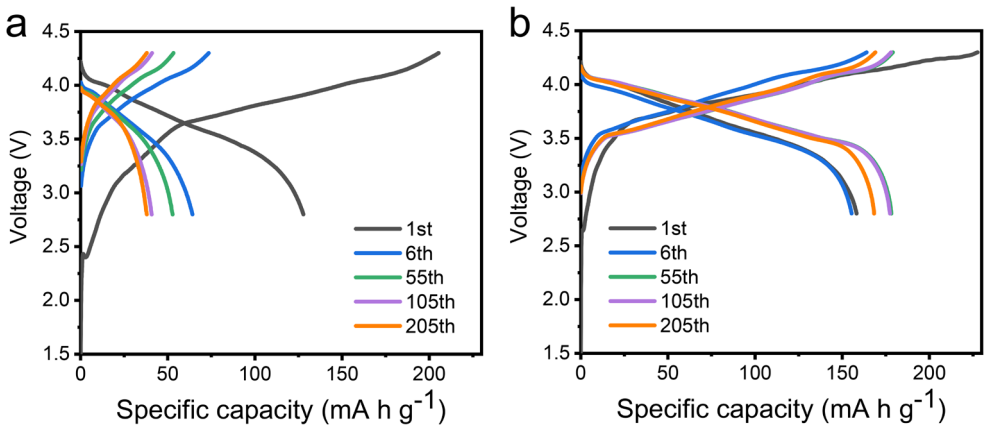

Figure S33. Voltage profiles of MCMB||NMC811 full-cells using BE + 2% VC (a) and LiFSI-TEOSCN (b) after exposing for 1 h in air atmosphere (Humidity: 50%, Temperature: 25 °C).

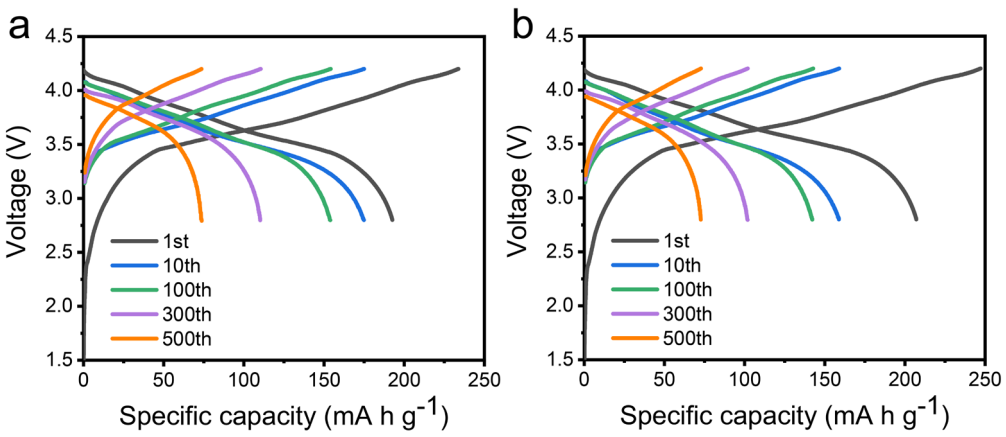

Figure S34. Voltage profiles of MCMB||NMC811 full-cells using BE (a) and BE + 2% VC (b) electrolytes between 2.8 V to 4.2 V at 60 °C.

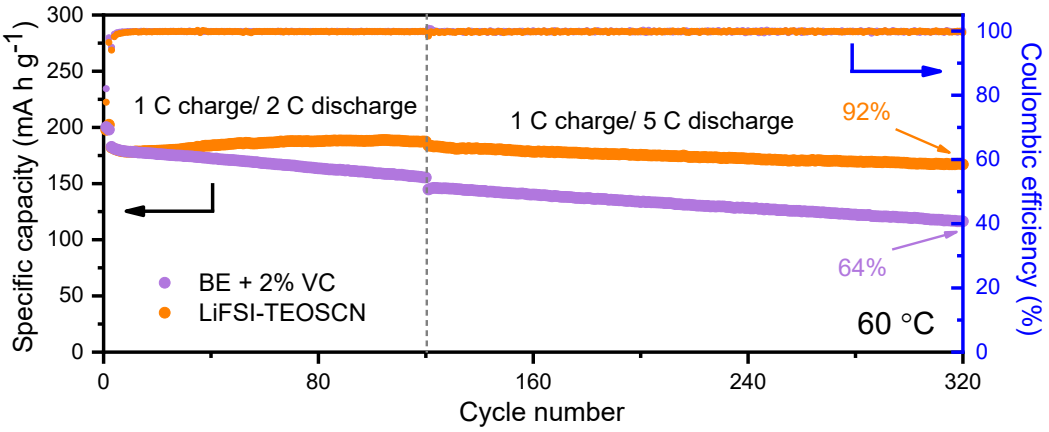

Figure S35. Cycling performance of MCMB||NMC811 full-cells using different electrolytes under 1 C charge / 2 C and 5 C discharge between 2.8 V to 4.2 V at 60 ℃.

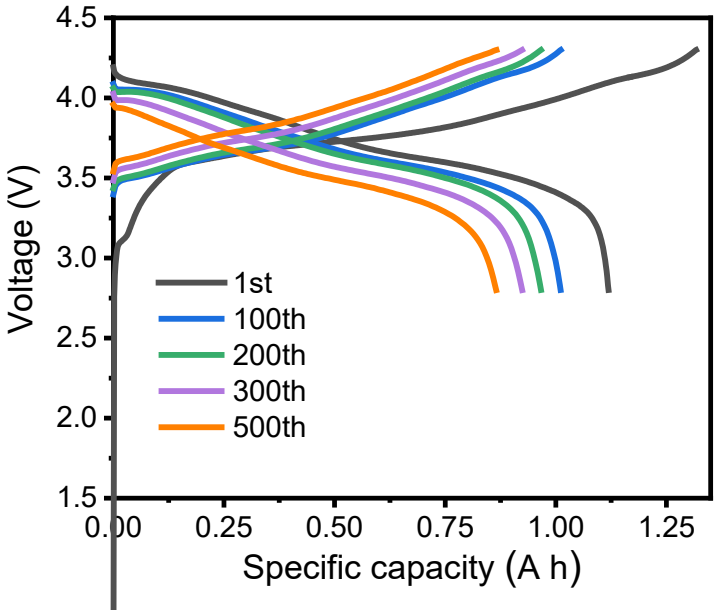

Figure S36. Voltage profiles of MCMB||NMC811 pouch cell using BE + 2% VC electrolyte between 2.8 V to 4.3 V at 25 ℃.

Abbreviations

LIBs	Lithium ion batteries	MD	molecular dynamics
SEI	solid electrolyte interphase	DFT	density functional theory
CEI	cathode electrolyte interphase	QC	Quantum chemistry
NMC	LiNixMnyCozO2	LSV	linear sweep voltammetry
LCO	LiCoO2	EIS	electrochemical impedance spectroscopy
LiFSI	Lithium bis(fluorosulfonyl)imide	ICP-MS	inductively coupled plasma mass spectrometry
$LiPF_6$	lithium hexafluorophosphate	NMR	nuclear magnetic resonance
TEOSCN	(2-cyanoethyl) triethoxysilane	XPS	X-ray photoelectron spectroscopy
EC/DMC	Ethylene carbonate/dimethyl carbonate	SEM	Scanning electron microscope
VC	vinylene carbonate	TEM	transmission electron microscopy
HF	hydrofluoric acid	HAADF	high angle annular dark field
TM	transition metal ion	Cryo-HRTEM	cryogenic high resolution transmission electron microscopy
HCEs	high concentration electrolytes	STEM-EELS	scanning transmission electron microscopy-electron energy loss spectroscopy
LHCEs	localized high concentration electrolytes		
SSIP/CIP/AGG	Solvent separated ion pair/contact ion pair/ion aggregate	*in situ* DEMS	*in situ* differential electrochemical mass spectrometry

Figure S37. Summary of all abbreviations in this article.

References

1 A. Austin, G. A. Petersson, M. J. Frisch, F. J. Dobek, G. Scalmani and K. Throssell, *J. Chem. Theory Comput.*, 2012, **8**, 4989-5007.

2 R. Peverati and D. G. Truhlar, *J. Phys. Chem. Lett*, 2017, **3**, 117-124.

3 A. Austin, G. A. Petersson, M. J. Frisch, F. J. Dobek, G. Scalmani and K. Throssell, *J. Chem. Theory Comput*, 2012, **8**, 4989-5007.

4 S. V. Sambasivarao and O. Acevedo, *J. Chem. Theory Comput.*, 2009, **5**, 1038–1050.

5 A. M. Tripathi, W. N. Su and B. J. Hwang, *Chem. Soc. Rev.*, 2018, **47**, 736-851.

6 B. Michalak, B. B. Berkes, H. Sommer, T. Brezesinski and J. Janek, *J. Phys. Chem. C*, 2016, **121**, 211-216.

7 D. Lu, G. Xu, Z. Hu, Z. Cui, X. Wang, J. Li, L. Huang, X. Du, Y. Wang, J. Ma, X. Lu, H. J. Lin, C. T. Chen, A. A. Nugroho, L. H. Tjeng and G. Cui, *Small Methods*, 2019, **3**, 1900546.

8 H. Wang, E. Rus, T. Sakuraba, J. Kikuchi, Y. Kiya and H. D. Abruna, *Anal. Chem.*, 2014, **86**, 6197-6201.

9 R. Bernhard, M. Metzger and H. A. Gasteiger, J. Electrochem. Soc., 2015, **162**, A1984-A1989.

10 K. Tasaki, *J. Phys. Chem. B*, 2005, **109**, 2920-2933.

11 R. Imhof and P. Novak, *J. Electrochem. Soc.* , 1998, **145**, 1081-1087.

12 L. L. Jiang, C. Yan, Y. X. Yao, W. Cai, J. Q. Huang and Q. Zhang, *Angew. Chem. Int. Ed.*, 2021, **60**, 3402-3406.

13 I. A. Shkrob, T. W. Marin, Y. Zhu and D. P. Abraham, *J. Phys. Chem. C*, 2014, **118**, 19661-19671.